Polarization-sensitive swept-source optical coherence tomography with continuous source polarization modulation

Masahiro Yamanari, Shuichi Makita, and Yoshiaki Yasuno

Computational Optics Group in the University of Tsukuba, Tsukuba, Ibaraki, Japan

yamanari@optlab2.bk.tsukuba.ac.jp

http://optics.bk.tsukuba.ac.jp/COG/

Abstract: We present fiber-based polarization-sensitive swept-source optical coherence tomography (SS-OCT) based on continuous source polarization modulation. The light source is a frequency swept laser centered at 1.31 μm with a scanning rate of 20 kHz. The incident polarization is modulated by a resonant electro-optic modulator at 33.3 MHz, which is one-third of the data acquisition frequency. The zeroth- and first-order harmonic components of the OCT signals with respect to the polarization modulation frequency have the polarimetric information of the sample. By algebraic and matrix calculations of the signals, this system can measure the depth-resolved Jones matrices of the sample with a single wavelength scan. The phase fluctuations of the starting trigger of wavelength scan and the polarization modulation are cancelled by monitoring the OCT phase of a calibration mirror inserted into the sample arm. We demonstrate the potential of the system by the measurement of chicken breast muscle and the volumetric measurement of an *in vivo* human anterior eye segment. The phase retardation image shows an additional contrast in the fibrous tissue such as the collagen fiber in the trabecular meshwork and sclera.

OCIS codes: (170.4500) Optical coherence tomography; (170.3880) Medical and biological imaging; (170.4460) Ophthalmic optics and devices; (260.5430) Polarization; (260.1440) Birefringence; (110.4500) Optical coherence tomography.

References and links

1. D. Huang, E. A. Swanson, C. P. Lin, J. S. Schuman, W. G. Stinson, W. Chang, M. R. Hee, T. Flotte, K. Gregory, C. A. Puliafito, and J. G. Fujimoto, "Optical coherence tomography," Science **254**, 1178–1181 (1991).
2. R. Leitgeb, C. Hitzenberger, and A. Fercher, "Performance of fourier domain vs. time domain optical coherence tomography," Opt. Express **11**, 889–894 (2003), http://www.opticsexpress.org/abstract.cfm?URI=oe-11-8-889.
3. J. F. de Boer, B. Cense, B. H. Park, M. C. Pierce, G. J. Tearney, and B. E. Bouma, "Improved signal-to-noise ratio in spectral-domain compared with time-domain optical coherence tomography," Opt. Lett. **28**, 2067–2069 (2003).
4. M. Choma, M. Sarunic, C. Yang, and J. Izatt, "Sensitivity advantage of swept source and Fourier domain optical coherence tomography," Opt. Express **11**, 2183–2189 (2003), http://www.opticsexpress.org/abstract.cfm?URI=oe-11-18-2183.
5. M. Wojtkowski, T. Bajraszewski, P. Targowski, and A. Kowalczyk, "Real-time in vivo imaging by high-speed spectral optical coherence tomography," Opt. Lett. **28**, 1745–1747 (2003).

#92281 - $15.00 USD Received 30 Jan 2008; revised 22 Mar 2008; accepted 8 Apr 2008; published 11 Apr 2008

6. N. Nassif, B. Cense, B. H. Park, S. H. Yun, T. C. Chen, B. E. Bouma, G. J. Tearney, and J. F. de Boer, "In vivo human retinal imaging by ultrahigh-speed spectral domain optical coherence tomography," Opt. Lett. **29**, 480–482 (2004).
7. S. Yun, G. Tearney, J. de Boer, N. Iftimia, and B. Bouma, "High-speed optical frequency-domain imaging," Opt. Express **11**, 2953–2963 (2003), http://www.opticsexpress.org/abstract.cfm?URI=oe-11-22-2953.
8. S. Yun, G. Tearney, B. Bouma, B. Park, and J. de Boer, "High-speed spectral-domain optical coherence tomography at 1.3 μm wavelength," Opt. Express **11**, 3598–3604 (2003), http://www.opticsexpress.org/abstract.cfm?URI=oe-11-26-3598.
9. R. Huber, D. C. Adler, and J. G. Fujimoto, "Buffered Fourier domain mode locking: unidirectional swept laser sources for optical coherence tomography imaging at 370,000 lines/s," Opt. Lett. **31**, 2975–2977 (2006).
10. M. R. Hee, D. Huang, E. A. Swanson, and J. G. Fujimoto, "Polarization-sensitive low-coherence reflectometer for birefringence characterization and ranging," J. Opt. Soc. Am. B **9**, 903–908 (1992).
11. J. F. de Boer, T. E. Milner, M. J. C. van Gemert, and J. S. Nelson, "Two-dimensional birefringence imaging in biological tissue by polarization-sensitive optical coherence tomography," Opt. Lett. **22**, 934–936 (1997).
12. B. Cense, T. C. Chen, B. H. Park, M. C. Pierce, and J. F. de Boer, "Thickness and birefringence of healthy retinal nerve fiber layer tissue measured with polarization-sensitive optical coherence tomography," Invest. Ophthalmol. Vis. Sci. **45**, 2606–2612 (2004).
13. M. C. Pierce, J. Strasswimmer, B. H. Park, B. Cense, and J. F. de Boer, "Advances in optical coherence tomography imaging for dermatology," J. Invest. Dermatol. **123**, 458–463 (2004).
14. W. Drexler, D. Stamper, C. Jesser, X. Li, C. Pitris, K. Saunders, S. Martin, M. B. Lodge, J. G. Fujimoto, and M. E. Brezinski, "Correlation of collagen organization with polarization sensitive imaging of in vitro cartilage: implications for osteoarthritis," J. Rheumatol. **28**, 1311–1318 (2001).
15. D. Fried, J. Xie, S. Shafi, J. D. B. Featherstone, T. M. Breunig, and C. Le, "Imaging caries lesions and lesion progression with polarization sensitive optical coherence tomography," J. Biomed. Opt. **7**, 618–627 (2002).
16. J. J. Pasquesi, S. C. Schlachter, M. D. Boppart, E. Chaney, S. J. Kaufman, and S. A. Boppart, "*In vivo* detection of exercised-induced ultrastructural changes in genetically-altered murine skeletal muscle using polarization-sensitive optical coherence tomography," Opt. Express **14**, 1547–1556 (2006), http://www.opticsexpress.org/abstract.cfm?URI=oe-14-4-1547.
17. C. Hitzenberger, E. Goetzinger, M. Sticker, M. Pircher, and A. Fercher, "Measurement and imaging of birefringence and optic axis orientation by phase resolved polarization sensitive optical coherence tomography," Opt. Express **9**, 780–790 (2001), http://www.opticsexpress.org/abstract.cfm?URI=oe-9-13-780.
18. G. Yao and L. V. Wang, "Two-dimensional depth-resolved Mueller matrix characterization of biological tissue by optical coherence tomography," Opt. Lett. **24**, 537–539 (1999).
19. S. Jiao and L. V. Wang, "Two-dimensional depth-resolved Mueller matrix of biological tissue measured with double-beam polarization-sensitive optical coherence tomography," Opt. Lett. **27**, 101–103 (2002).
20. Y. Yasuno, S. Makita, Y. Sutoh, M. Itoh, and T. Yatagai, "Birefringence imaging of human skin by polarization-sensitive spectral interferometric optical coherence tomography," Opt. Lett. **27**, 1803–1805 (2002).
21. Y. Yasuno, S. Makita, T. Endo, M. Itoh, T. Yatagai, M. Takahashi, C. Katada, and M. Mutoh, "Polarization-sensitive complex Fourier domain optical coherence tomography for Jones matrix imaging of biological samples," Appl. Phys. Lett. **85**, 3023–3025 (2004).
22. E. Götzinger, M. Pircher, and C. K. Hitzenberger, "High speed spectral domain polarization sensitive optical coherence tomography of the human retina," Opt. Express **13**, 10,217–10,229 (2005), http://www.opticsexpress.org/abstract.cfm?URI=oe-13-25-10217.
23. C. E. Saxer, J. F. de Boer, B. H. Park, Y. Zhao, Z. Chen, and J. S. Nelson, "High-speed fiber based polarization-sensitive optical coherence tomography of in vivo human skin," Opt. Lett. **25**, 1355–1357 (2000).
24. J. E. Roth, J. A. Kozak, S. Yazdanfar, A. M. Rollins, and J. A. Izatt, "Simplified method for polarization-sensitive optical coherence tomography," Opt. Lett. **26**, 1069–1071 (2001).
25. B. H. Park, M. C. Pierce, B. Cense, and J. F. de Boer, "Jones matrix analysis for a polarization-sensitive optical coherence tomography system using fiber-optic components," Opt. Lett. **29**, 2512–2514 (2004).
26. S. Jiao, W. Yu, G. Stoica, and L. V. Wang, "Optical-fiber-based Mueller optical coherence tomography," Opt. Lett. **28**, 1206–1208 (2003).
27. S. Jiao, M. Todorović, G. Stoica, and L. V. Wang, "Fiber-based polarization-sensitive Mueller matrix optical coherence tomography with continuous source polarization modulation," Appl. Opt. **44**, 5463–5467 (2005).
28. J. Zhang, W. Jung, J. Nelson, and Z. Chen, "Full range polarization-sensitive Fourier domain optical coherence tomography," Opt. Express **12**, 6033–6039 (2004), http://www.opticsexpress.org/abstract.cfm?URI=oe-12-24-6033.
29. B. Park, M. C. Pierce, B. Cense, S.-H. Yun, M. Mujat, G. Tearney, B. Bouma, and J. de Boer, "Real-time fiber-based multi-functional spectral-domain optical coherence tomography at 1.3 μm," Opt. Express **13**, 3931–3944 (2005), http://www.opticsexpress.org/abstract.cfm?URI=oe-13-11-3931.
30. B. Cense, "Optical coherence tomography for retinal imaging," Ph.D. thesis, Twente University (2005).
31. M. Yamanari, S. Makita, V. D. Madjarova, T. Yatagai, and Y. Yasuno, "Fiber-based polarization-sensitive Fourier domain optical coherence tomography using B-scan-oriented polarization modulation method," Opt. Express **14**,

#92281 - $15.00 USD Received 30 Jan 2008; revised 22 Mar 2008; accepted 8 Apr 2008; published 11 Apr 2008

6502–6515 (2006), http://www.opticsexpress.org/abstract.cfm?URI=oe-14-14-6502.
32. W. Oh, S. Yun, B. Vakoc, M. Shishkov, A. Desjardins, B. Park, J. de Boer, G. Tearney, and B. Bouma, "High-speed polarization sensitive optical frequency domain imaging with frequency multiplexing," Opt. Express **16**, 1096–1103 (2008), http://www.opticsexpress.org/abstract.cfm?URI=oe-16-2-1096.
33. M. Yamanari, M. Miura, S. Makita, T. Yatagai, and Y. Yasuno, "Phase retardation measurement of retinal nerve fiber layer by polarization-sensitive spectral-domain optical coherence tomography and scanning laser polarimetry," J. Biomed. Opt. **13**, 014013 (2008).
34. Y. Yasuno, V. D. Madjarova, S. Makita, M. Akiba, A. Morosawa, C. Chong, T. Sakai, K.-P. Chan, M. Itoh, and T. Yatagai, "Three-dimensional and high-speed swept-source optical coherence tomography for in vivo investigation of human anterior eye segments," Opt. Express **13**, 10,652–10,664 (2005), http://www.opticsexpress.org/abstract.cfm?URI=oe-13-26-10652.
35. B. Vakoc, S. Yun, J. de Boer, G. Tearney, and B. Bouma, "Phase-resolved optical frequency domain imaging," Opt. Express **13**, 5483–5493 (2005), http://www.opticsexpress.org/abstract.cfm?URI=oe-13-14-5483.
36. M. Pierce, M. Shishkov, B. Park, N. Nassif, B. Bouma, G. Tearney, and J. de Boer, "Effects of sample arm motion in endoscopic polarization-sensitive optical coherence tomography," Opt. Express **13**, 5739–5749 (2005), http://www.opticsexpress.org/abstract.cfm?URI=oe-13-15-5739.
37. M. Pircher, E. Gotzinger, B. Baumann, and C. K. Hitzenberger, "Corneal birefringence compensation for polarization sensitive optical coherence tomography of the human retina," J. Biomed. Opt. **12**, 041210 (2007).
38. J. Zhang and Z. Chen, "In vivo blood flow imaging by a swept laser source based Fourier domain optical Doppler tomography," Opt. Express **13**, 7449–7457 (2005), http://www.opticsexpress.org/abstract.cfm?URI=oe-13-19-7449.
39. M. Todorović, S. Jiao, L. V. Wang, and G. Stoica, "Determination of local polarization properties of biologicalsamples in the presence of diattenuation by use of Muelleroptical coherence tomography," Opt. Lett. **29**, 2402–2404 (2004).
40. M. Pircher, E. Goetzinger, R. Leitgeb, and C. K. Hitzenberger, "Transversal phase resolved polarization sensitive optical coherence tomography," Phys. Med. Biol. **49**, 1257–1263 (2004).
41. Y. Chen, D. M. de Bruin, C. Kerbage, and J. F. de Boer, "Spectrally balanced detection for optical frequency domain imaging," Opt. Express **15**, 16,390–16,399 (2007), http://www.opticsexpress.org/abstract.cfm?URI=oe-15-25-16390.

1. Introduction

Optical coherence tomography (OCT) is an interferometric imaging technique for the non-invasive measurement of biological samples [1]. Recent developments in the spectral-domain (SD) and swept-source (SS) OCT have dramatically improved the sensitivity [2, 3, 4]. Subsequently, high-speed OCT systems have been demonstrated [5, 6, 7, 8, 9]. As a functional extension of OCT, polarization-sensitive OCT (PS-OCT) has been developed to measure the depth-resolved birefringence of biological tissues [10, 11]. PS-OCT has a unique and powerful characteristic to detect and analyze fibrous tissues, e.g., retinal nerve fiber layer [12], collagen fiber in skin [13] and cartilage [14], caries lesions [15] and skeletal muscle [16].

Several methods and algorithms have been developed for PS-OCT. Free-space PS-OCT with a circularly polarized incident beam and polarization-sensitive detection is the simplest way to detect the phase retardation and orientation of the sample [17]. The Mueller matrix or Jones matrix represents complete polarimetric information of the sample, and they can be measured using several different states of the incident polarization [18, 19]. Yasuno et al. first implemented free-space PS-OCT with SD-OCT to measure the Mueller or Jones matrices of the sample. [20, 21]. High-speed free-space PS-SD-OCT with a circularly polarized incident beam has been demonstrated by Götzinger et al. for retinal imaging [22]. To maintain the stable state of polarization in PS-OCT systems, the optical components have to be fixed mechanically. Therefore, free-space optical systems are more appropriate than optical-fiber-based systems. Although the calculation of birefringence becomes simple, the flexibility of the measurement, which is highly desired for medical examinations, is sacrificed.

In order to use fiber-optic components for PS-OCT, several algorithms have been developed, for example, the Stokes vector method [23], algebraic manipulation method with polarization-sensitive bulk optics in the sample arm [24], and Jones matrix method with sequential polar-

#92281 - $15.00 USD Received 30 Jan 2008; revised 22 Mar 2008; accepted 8 Apr 2008; published 11 Apr 2008

ization modulation [25]. These methods require multiple depth scans with different incident polarizations at the same position. This is because the first method needs to determine the rotating plane of the Stokes vectors on the Poincaré sphere, the second method needs to measure sufficient depth scans for algebraic manipulation, and the third method needs to measure all the complete four elements of a Jones matrix. This requirement results in a slower effective line rate for the calculation of the birefringence.

To overcome this restriction of fiber-based PS-OCT, certain methods were developed. Jiao et al. developed fiber-based PS-OCT with two superposed light sources [26] and continuous polarization modulation [27] based on the time-domain OCT technique. Although fiber-based spectral-domain or swept-source PS-OCT was recently developed to achieve high sensitivity and resultant high imaging speed [28, 29, 30, 31, 32], only a system develeped by Oh et al. [32] can measure birefringence of a sample with a single wavelength scan. The other fiber-based spectral-domain or swept-source PS-OCT systems alter the incident polarization for each depth scan. Therefore, the disadvantage of the line rate still remains. In the case of our previous PS-SD-OCT system [31], since it utilized a phase modulation along the transversal scanning direction, a displacement of the scatterer caused an artifitial birefringence [33], and it required a highly dense transversal scan to maintain the correlation between adjacent depth scans.

In this paper, we present a fiber-based PS-SS-OCT system based on a novel algorithm using continuous polarization modulation. The incident polarization is modulated at one-third of the frequency of the data acquisition. It generates frequency-shifted OCT signals with respect to the modulation frequency. Since this method can provide the Jones matrix of the sample with a single wavelength-scan, our PS-SS-OCT system does not have the abovementioned limitations. We describe the details of the system and theory in Section 2 and show the intensity, phase retardation and orientation images of chicken breast muscle and an *in vivo* anterior eye segment in Section 3.

2. System and theory

2.1. System configuration

Figure 1 shows the schematic of the system. The light source is a commercially available scanning laser (HSL-2000, Santec, Japan). A standard SS-OCT system with this light source was reported previously [34]. The light source sweeps the wavelength at a line rate of 20 kHz over a span of 110 nm centered at 1.31 μm. The output power is 5.4 mW, and the lasing duty cycle is 50%. The light is polarized by a linear polarizer (LP) at 90° and modulated by a resonant electro-optic modulator (EOM) with an optic axis of 45° (EO-AM-R-033.3-C3, Nova Phase, Inc). The EOM sinusoidally modulates the phase retardation between the horizontal and vertical polarizations of light at a frequency of 33.3 MHz and a modulation amplitude of 2.405 radians. A function generator (33250A, Agilent Inc) and an RF amplifier (RFAMP-150, Nova Phase, Inc) with a voltage gain of 25.5 dB drive the EOM. The modulated light is coupled to a single mode fiber coupler. 10% of this modulated light is directed to the reference arm and 90% to the sample arm. In the reference arm, in-line polarization controllers (PC) and an LP have a role in obtaining a constant optical power and a constant state of polarization at the reference arm independent of the incident polarization modulation by the EOM. For this purpose, a photodetector connected to an oscilloscope in the reference arm monitors the optical power, and is utilized in aligning of the PCs and LP. The reference light is then coupled to a polarization-maintaining fiber (PMF). In the sample arm, 99% of the light illuminates the sample through a two-axis galvanometer scanner and an objective lens with a 60 mm focal length. The theoretical transversal resolution at the focus is 32.2 μm. 1% of the probing light is directed to a mirror in order to provide a calibration signal for the timing-phase difference between the EOM and the data acquisition of each spectral acquisition. The details of this active calibration are

#92281 - $15.00 USD Received 30 Jan 2008; revised 22 Mar 2008; accepted 8 Apr 2008; published 11 Apr 2008

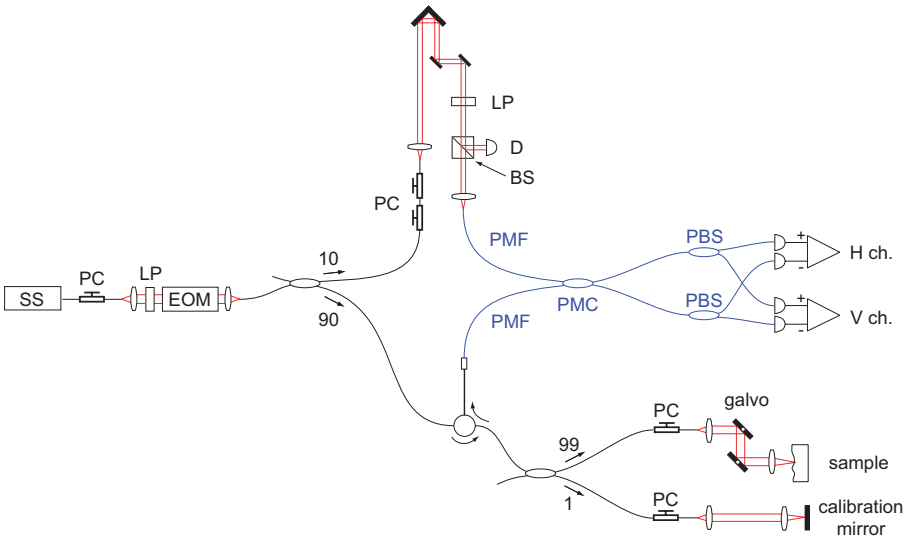

Fig. 1. Schematic of the system. SS: frequency swept laser source, PC: in-line polarization controller, LP: linear polarizer, EOM: electro-optic modulator, D: photodetector, BS: nonpolarizing beamsplitter, PMF: polarization-maintaining fiber, PMC: polarization-maintaining coupler, PBS: in-line fiber-optic polarizing beamsplitter, H ch.: balanced photoreceiver of horizontally polarized light channel, V ch.: balanced photoreceiver of vertically polarized light channel.

described in Section 2.3. Back-reflected light from the sample arm is coupled to the PMF. The reference and sample beams are directed to a polarization-maintaining fiber coupler (PMC) and interfered with each other. In-line fiber-optic polarizing beamsplitters (PBSs) are attached to the two output ports of the PMC. The horizontally and vertically polarized signals are detected by two balanced photoreceivers (Model 1817, New Focus, Inc.). The detected signals are bandpass filtered from 300 kHz to 55 MHz and amplified electrically. A data acquisition board (Octopus CS8349, Gage Applied Technologies, Inc.) acquires the data at 100 MS/s.

2.2. Principle of polarization-sensitive detection

In this subsection, we first describe the polarization in the system using the Jones formalism. Then, we derive the birefringence of the sample. Although our method is similar to the methods demonstrated previously [27, 31], there are several important different points. In order to avoid the confusion, we explain the details thoroughly.

The phase modulation of the EOM is

$$\varphi = A_0 \sin(\omega_m t), \tag{1}$$

where $A_0 = 2.405$ radians and ω_m is the frequency of the polarization modulation. The Jones matrix of the EOM with the fast axis of $\pi/4$ can be written as

$$\begin{pmatrix} \cos\frac{\varphi}{2} & i\sin\frac{\varphi}{2} \\ i\sin\frac{\varphi}{2} & \cos\frac{\varphi}{2} \end{pmatrix}. \tag{2}$$

By applying Eq. (2) to the Jones vector of the vertically polarized light, the Jones vector of the

#92281 - $15.00 USD Received 30 Jan 2008; revised 22 Mar 2008; accepted 8 Apr 2008; published 11 Apr 2008

light after athe modulation by the EOM is derived as

$$\begin{pmatrix} H_i \\ V_i \end{pmatrix} = \begin{pmatrix} i\sin\frac{\varphi}{2} \\ \cos\frac{\varphi}{2} \end{pmatrix}. \tag{3}$$

We define the Jones matrix that accounts for the birefiringence of the fiber-optic components and the sample as

$$\mathbf{J}_{\text{all}} = \mathbf{J}_{\text{out}}\mathbf{J}_{\text{sam}}\mathbf{J}_{\text{in}} = \begin{pmatrix} j_{1,1} & j_{1,2} \\ j_{2,1} & j_{2,2} \end{pmatrix}, \tag{4}$$

where $\mathbf{J}_{\text{in}}$ is a Jones matrix from the EOM to the sample surface, $\mathbf{J}_{\text{sam}}$ is a depth-dependent double-pass Jones matrix of the sample, which we want to determine, and $\mathbf{J}_{\text{out}}$ is a Jones matrix from the sample surface to the PMC. The Jones vector of light from the sample at the PMC can be represented as

$$\begin{pmatrix} H_{\text{sam}} \\ V_{\text{sam}} \end{pmatrix} = \mathbf{J}_{\text{all}} \begin{pmatrix} H_i \\ V_i \end{pmatrix} = \begin{pmatrix} j_{1,2}\cos\frac{\varphi}{2} + ij_{1,1}\sin\frac{\varphi}{2} \\ j_{2,2}\cos\frac{\varphi}{2} + ij_{2,1}\sin\frac{\varphi}{2} \end{pmatrix} \tag{5}$$

The Jones vector of the reference light at the PMC can be represented as

$$\mathbf{E}_{\text{ref}} = \begin{pmatrix} H_{\text{ref}} \\ V_{\text{ref}} \end{pmatrix} = \begin{pmatrix} H_r \\ V_r \end{pmatrix} e^{-i\frac{\varphi}{2}}, \tag{6}$$

where H_r and V_r represent the phase constants without the polarization modulation. The horizontally polarized component of the interference signal of the reference and sample beams at the detection arm is

$$I_h(t) = |H_{\text{ref}}|^2 + |H_{\text{sam}}|^2 + H_{\text{ref}}(t)H^*_{\text{sam}}(t) + c.c., \tag{7}$$

where *c.c.* denotes the complex conjugate of the third term. The first and second terms are suppressed by the balanced photoreceiver. The third and *c.c.* terms represent the OCT signal and its mirror corresponds to the positive and negative frequency components of the spectral interference signal. The path length of the reference arm is adjusted so that the positive and negative frequency terms of the OCT signal do not overlap with each other in the axial depth range. Therefore, we consider only the third term in the following equations. The detected signal $I_h(t)$ is Fourier transformed and rearranged as

$$\tilde{I}_h(\tilde{t}) = \mathscr{F}[H_{\text{ref}}(t)H^*_{\text{sam}}(t)] = \frac{H_r}{2}\{\mathscr{F}[j^*_{1,2} - j^*_{1,1}] + \mathscr{F}[j^*_{1,2} + j^*_{1,1}] * \mathscr{F}[e^{-i\varphi}]\}, \tag{8}$$

where $\tilde{I}_h$ denotes the interference part of the signal, $\tilde{t}$ is the Fourier conjugate of t, and $\mathscr{F}[\cdot]$ and $*$ denote the Fourier transform from time to its Fourier spectral domain and a convolution operator, respectively. Here, we have to note that the spectral interference signal obtained is not rescaled to the optical frequency domain. This is because the polarization modulation of the probe beam is even in the sampling timing. The second term was shifted in the $\tilde{t}$ domain because of the polarization modulation by the EOM. $\mathscr{F}[e^{-i\varphi}]$ can be rearranged as

$$\begin{aligned} \mathscr{F}[e^{-i\varphi}] = \sum_{l=0}^{\infty} \big[& J_{2l}(A_0)\{\delta(k-2l\omega_m) + \delta(k+2l\omega_m)\} \\ & - J_{2l+1}(A_0)\{\delta(k-(2l+1)\omega_m) + \delta(k+(2l+1)\omega_m)\}\big], \end{aligned} \tag{9}$$

using the expansion of the Bessel functions to the trigonometric terms,

$$\begin{cases} \sin[\varphi(t)] = \sum_{l=0}^{\infty} 2J_{2l+1}(A_0)\sin[(2l+1)\omega_m t] \\ \cos[\varphi(t)] = J_0(A_0) + \sum_{l=1}^{\infty} 2J_{2l}(A_0)\cos[(2l)\omega_m t] \end{cases} \tag{10}$$

#92281 - $15.00 USD Received 30 Jan 2008; revised 22 Mar 2008; accepted 8 Apr 2008; published 11 Apr 2008

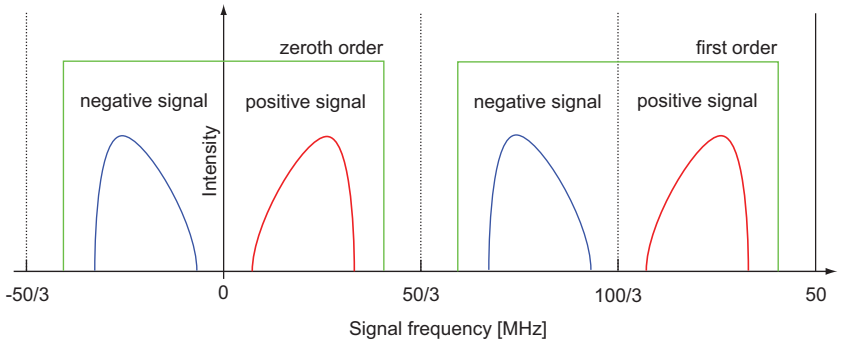

Fig. 2. Diagram of the detected signal after Fourier transform.

where the italicized capital letters $J_0(A_0)$, $J_{2l}(A_0)$, and $J_{2l+1}(A_0)$ are the Bessel functions of the first kind of the order of $0, 2l$, and $2l+1$, respectively. Since we set $A_0 = 2.405$ radians, the zeroth-order Bessel function disappears, namely, $J_0(A_0) = 0$. Equations (8) and (9) suggest that the zeroth ($l = 0$) and first ($l = 1$) order terms are distinctive in the Fourier-spectrum space, and we can distinguish these two signals as

$$\tilde{I}_{h0}(z) = \frac{H_r}{2}(j^*_{1,2} - j^*_{1,1}), \tag{11}$$

$$\tilde{I}_{h1}(z) = -\frac{J_1(A_0)H_r}{2}(j^*_{1,2} + j^*_{1,1}), \tag{12}$$

where $\tilde{I}_{h0}(z)$ and $\tilde{I}_{h1}(z)$ are the zeroth- and first-order horizontally polarized OCT signals, respectively.

Figure 2 shows the schematic diagram of the detected signal in the Fourier-spectral domain. Since the detected signals are of real values, the zeroth-order signal has positive and negative frequency components close to the zero depth. The polarization modulation generates the $\pm$ first-order signals with respect to the frequency of the EOM (the negative first-order signal is not shown in Fig. 2). The zeroth- and first-order complex signals correspond to the first row of the Jones matrix as shown in Eqs. (11) and (12). In the Fourier-spectral domain shown in Fig. 2, they are windowed and extracted individually. The first-order signal is then shifted so that the frequency of the polarization modulation is demodulated. The zeroth-order and the shifted first-order signals are individually inverse Fourier transformed to the original detection domain, which results in complex interference spectra. The real and imaginary parts of the complex spectra of the zeroth- and first-order signals are individually rescaled in order to calibrate the nonlinearlity of the frequency sweeping of the light source. Finally, two complex spectral interference signals linearly tuned in the optical frequency are obtained.

When the path lengths of the PMF in the reference and sample arms are different, there arises a difference between the path lengths of horizontally and vertically polarized OCT signals. This is because the refractive indices of horizontally and vertically polarized modes in the PMF are different. It is compensated for by accuracy higher than a single pixel through the numerical adjustment of the first-order dispersions to the horizontally and vertically polarized spectra individually. The remaining path-length mismatch between the horizontally and vertically polarized OCT signals results in the constant phase accounted by H_r and V_r. Hence, we can safely ignore it, as described later.

The mismatch of the second-order dispersion between the reference arm and the sample arm

#92281 - $15.00 USD Received 30 Jan 2008; revised 22 Mar 2008; accepted 8 Apr 2008; published 11 Apr 2008

is compensated numerically for all spectra. The compensated spectra are Fourier transformed, and the depth-resolved signals $\tilde{I}_{h0}(z)$ and $\tilde{I}_{h1}(z)$ are obtained.

In our implementation, the signal stability of the first-order negative signal is higher than that of the first-order positive signal because of the noise properties of the system. Therefore, the zeroth- and first-order negative signals are used for the calculation.

Equations (11) and (12) are rearranged in order to obtain two elements of the Jones matrix $\mathbf{J}_{\text{all}}$ as

$$H_r j_{1,1}^* = -\left(\tilde{I}_{h0} + \frac{\tilde{I}_{h1}}{J_1(A_0)}\right), \tag{13}$$

$$H_r j_{1,2}^* = \tilde{I}_{h0} - \frac{\tilde{I}_{h1}}{J_1(A_0)}. \tag{14}$$

In the same manner, the other two elements of the Jones matrix can be calculated using the vertically polarized signals as

$$V_r j_{2,1}^* = -\left(\tilde{I}_{v0} + \frac{\tilde{I}_{v1}}{J_1(A_0)}\right), \tag{15}$$

$$V_r j_{2,2}^* = \tilde{I}_{v0} - \frac{\tilde{I}_{v1}}{J_1(A_0)}. \tag{16}$$

We obtain the Jones matrix $\mathbf{J}_{\text{measured}}$ by combining Eqs. (13), (14), (15), and (16) as

$$\mathbf{J}_{\text{measured}} = \begin{pmatrix} H_r^* & 0 \\ 0 & V_r^* \end{pmatrix} \begin{pmatrix} -\left(\tilde{I}_{h0}^* + \frac{\tilde{I}_{h1}^*}{J_1(A_0)}\right) & \tilde{I}_{h0}^* - \frac{\tilde{I}_{h1}^*}{J_1(A_0)} \\ -\left(\tilde{I}_{v0}^* + \frac{\tilde{I}_{v1}^*}{J_1(A_0)}\right) & \tilde{I}_{v0}^* - \frac{\tilde{I}_{v1}^*}{J_1(A_0)} \end{pmatrix}. \tag{17}$$

We set the LP and PC in the reference arm in order to satisfy the condition $|H_r| = |V_r|$. Hence, we can omit the amplitudes of the first matrix on the right-hand side of Eq. (17). It is arranged as

$$\mathbf{J}_{\text{offset}} = \begin{pmatrix} 1 & 0 \\ 0 & e^{i\gamma} \end{pmatrix}, \tag{18}$$

where $e^{i\gamma} = \angle(V_r^*) - \angle(H_r^*)$. $\mathbf{J}_{\text{offset}}$ describes the constant phase offset between the horizontally and vertically polarized signals due to an effect of the PMF in the reference and sample arms. Equation (18) is clearly a unitary matrix. The measured Jones matrix can be described as

$$\mathbf{J}_{\text{measured}} = \mathbf{J}_{\text{offset}} \mathbf{J}_{\text{all}}. \tag{19}$$

Assuming that fiber-optic components have no diattenuation, $\mathbf{J}_{\text{in}}$ and $\mathbf{J}_{\text{out}}$ can be characterized as elliptic retarders, namely, unitary matrices. In order to compensate the effects of the fiber-optic components, namely, $\mathbf{J}_{\text{in}}, \mathbf{J}_{\text{out}}$ and $\mathbf{J}_{\text{offset}}$, we apply the matrix diagonalization method developed by Park et al. [25] These procedures finally provide the phase retardation, diattenuation, and relative orientation of the sample.

2.3. Calibration of phase fluctuation

Since the PS-SS-OCT is a phase-sensitive system, the phase fluctuation results in an artifact of the measurement. The sources of the phase fluctuation are the jitter of the start trigger of the wavelength sweeping generated by the light source, which we define as A-trigger, and the asynchronous driving between the data acquisition and the polarization modulation by the EOM. In this subsection, we describe how they affect the system and how they can be cancelled.

#92281 - $15.00 USD Received 30 Jan 2008; revised 22 Mar 2008; accepted 8 Apr 2008; published 11 Apr 2008

The DAQ receives an A-trigger from the light source and starts the acquisition. The A-trigger has a fluctuation in the timing because it is generated by a photodetector equipped with a narrow optical bandpass filter and is not sufficiently accurate to be synchronized with the timing clock of the DAQ. The A-trigger fluctuation in successive depth scans causes the phase error among the OCT signals that linearly increases to the axial depth. Both zeroth- and first-order OCT signals are affected by the same phase error. Vakoc et al. have developed a method to compensate the A-trigger fluctuation [35]. In their method, a calibration mirror in the sample arm is used as a phase reference. We apply a modified version of their method to our system.

According to the shift theorem of the Fourier transform, the phase error can be written as $\exp\{-i2\alpha z\varepsilon(n)\}$, where α is the wavenumber-sweeping rate of the light source ($-1.6\cdot 10^{10}$ $\mathrm{m}^{-1}\mathrm{s}^{-1}$) and $\varepsilon(n)$ is the acquisition timing offset of the n-th depth scan. The zeroth-order horizontally polarized OCT signal $\tilde{I}_{h0}$ is then rewritten as $\exp\{-i2\alpha z\varepsilon(n)\}\tilde{I}_{h0}$. The other OCT signals $\tilde{I}_{h1}, \tilde{I}_{v0}$, and $\tilde{I}_{v1}$ are also affected by the same phase fluctuation. From Eq. (17), the phase error is common for all elements of $\mathbf{J}_{\mathrm{all}}$, namely,

$$\mathbf{J}'_{\mathrm{measured}} = e^{i2\alpha z\varepsilon(n)}\mathbf{J}_{\mathrm{measured}} = e^{i2\alpha z\varepsilon(n)}\mathbf{J}_{\mathrm{offset}}\mathbf{J}_{\mathrm{all}}. \tag{20}$$

Hence, the A-trigger fluctuation does not change any property of $\mathbf{J}'_{\mathrm{measured}}$ in the sense of a Jones matrix.

The second source of the phase fluctuation is the phase difference between the DAQ and the EOM. The light source has a polygon mirror scanner and the EOM is driven by a resonant electric circuit. Since these devices cannot be controlled externally during the resonant driving, it is difficult to synchronize them. Therefore, they are not synchronized in our system. This induces a phase offset to the polarization modulation. Equation (1) is rewritten as

$$\varphi' = A_0\sin(\omega_m t - \delta(n)), \tag{21}$$

where $\delta(n)$ is the phase offset of the n-th depth scan. Subsequently, equation (8) is rewritten as

$$\tilde{I}_h(z) = \frac{H_r}{2}\{\mathscr{F}[j^*_{1,2} - j^*_{1,1}] + e^{i\delta(n)}\mathscr{F}[j^*_{1,2} + j^*_{1,1}] * \mathscr{F}[e^{-i\varphi}]\}. \tag{22}$$

Equation (22) shows that the phase offset of the polarization modulation causes a depth-independent phase offset of the first-order signal. From Eqs. (17) and (20), the measured Jones matrix can be rewritten and rearranged to factorize the term involving $\delta(n)$ as

$$\begin{aligned}\mathbf{J}''_{\mathrm{measured}} &= e^{i2\alpha z\varepsilon(n)}\mathbf{J}_{\mathrm{offset}}\begin{pmatrix} -\left(\tilde{I}^*_{h0} + \frac{e^{-i\delta(n)}\tilde{I}^*_{h1}}{J_1(A_0)}\right) & \tilde{I}^*_{h0} - \frac{e^{-i\delta(n)}\tilde{I}^*_{h1}}{J_1(A_0)} \\ -\left(\tilde{I}^*_{v0} + \frac{e^{-i\delta(n)}\tilde{I}^*_{v1}}{J_1(A_0)}\right) & \tilde{I}^*_{v0} - \frac{e^{-i\delta(n)}\tilde{I}^*_{v1}}{J_1(A_0)} \end{pmatrix} \\ &= e^{i2\alpha z\varepsilon(n)}\mathbf{J}_{\mathrm{offset}}\mathbf{J}_{\mathrm{all}}\mathbf{J}_{\mathrm{offset2}},\end{aligned} \tag{23}$$

where

$$\mathbf{J}_{\mathrm{offset2}} = \frac{1}{2}\begin{pmatrix} e^{-i\delta(n)}+1 & e^{-i\delta(n)}-1 \\ e^{-i\delta(n)}-1 & e^{-i\delta(n)}+1 \end{pmatrix}. \tag{24}$$

Note that Eq. (24) is a unitary matrix.

Equation (23) shows that the A-trigger fluctuation and phase difference between the DAQ and the EOM induce the depth-dependent global phase offset and the depth-independent unitary matrix. They have limited effects to the measured Jones matrix, because they generate no artifact after the matrix diagonalization for a single depth scan.

#92281 - $15.00 USD Received 30 Jan 2008; revised 22 Mar 2008; accepted 8 Apr 2008; published 11 Apr 2008

If the sample has reflective surfaces and does not have scattering material, e.g., waveplates, the sample birefringence can be calculated accurately for each depth scan without compensating the phase fluctuation. However, we have experienced that it is not always applicable for biological samples. When the surface Jones matrix is extracted from each depth scan of the biological sample, the speckle noise of the signal at the sample surface significantly degrades the phase retardation and orientation images because of the failure of the matrix diagonalization. In order to remove the artifact, previous reports applied averaging for the surface signals [23, 31, 36, 37]. However, the averaging of the surface Jones matrices had not been possible because of the phase fluctuation in our system. In addition, this phase fluctuation makes it impossible to remove the fixed pattern noise numerically. Therefore, we should compensate them.

To compensate the phase difference between DAQ and EOM, first we calculate the relative phase difference of the OCT signals from the calibration mirror between the zeroth and *n*-th depth scans,

$$e^{i\{\delta(n)-\delta(0)\}} = \left\{ \frac{e^{i\delta(n)}e^{-i2\alpha z\varepsilon(n)}\tilde{I}_{h1}}{e^{-i2\alpha z\varepsilon(n)}\tilde{I}_{h0}} \right\} \Bigg/ \left\{ \frac{e^{i\delta(0)}e^{-i2\alpha z\varepsilon(0)}\tilde{I}_{h1}}{e^{-i2\alpha z\varepsilon(0)}\tilde{I}_{h0}} \right\}. \tag{25}$$

The *n*-th depth scan is divided by Eq. (25) in order to eliminate $\delta(n)$ as

$$\frac{1}{e^{i\{\delta(n)-\delta(0)\}}} e^{i\delta(n)}e^{-i2\alpha z\varepsilon(n)}\tilde{I}_{h1} = e^{i\delta(0)}e^{-i2\alpha z\varepsilon(n)}\tilde{I}_{h1}. \tag{26}$$

To compensate the A-trigger fluctuation, we can use the zeroth-order calibration signal, because the zeroth-order signal is affected only by the A-trigger fluctuation. The counter phase is generated based on the zeroth-order calibration signal and is applied to all the OCT signals of $\tilde{I}_{h0}, \tilde{I}_{h1}, \tilde{I}_{v0}$, and $\tilde{I}_{v1}$. As a result, the zeroth- and first-order OCT signals are compensated as $\exp\{-i2\alpha z\varepsilon(0)\}\tilde{I}_{h0}$ and $\exp\{i\delta(0)\}\exp\{-i2\alpha z\varepsilon(0)\}\tilde{I}_{h1}$, respectively.

In practice, the A-trigger fluctuation is greater than one sampling time of the DAQ, approximately five sampling times (50 ns), due to the limited accuracy of the A-trigger generator equipped with the light source. This results in the phase wrapping ambiguity of the correction by the calibration mirror, because it locates at the deep position. Instead of a more accurate but expensive A-trigger source, such as what uses a fiber Bragg grating, we use a fixed pattern signal at a depth of 0.2 mm for a rough calibration of the A-trigger fluctuation. Subsequently, we use the calibration mirror at the deep position (3.7 mm) for a fine calibration. This two-step method can sufficiently calibrate the A-trigger fluctuation, which cannot be done with only a single calibration signal.

We measured a static mirror as a sample to confirm the calibration of the phase fluctuations. The probing light was attenuated by a neutral density filter. The galvanometer scanner was turned off. The sample and calibration mirror were placed at depths of 1.9 mm and 3.7 mm, respectively. The OCT signals $\tilde{I}_{h0}$ and $\tilde{I}_{h1}$ of the calibration mirror with signal-to-noise ratios (SNRs) of 33.2 dB and 26.8 dB, respectively, were used to cancel the phase fluctuations. The signal phases of 512 depth scans were acquired at the depth of the sample. The standard deviations of the phases of $\tilde{I}_{h0}$, $\tilde{I}_{v0}$, $\tilde{I}_{h1}$, and $\tilde{I}_{v1}$ of the sample were 0.040, 0.042, 0.055, and 0.055 (rad) with SNRs of 41.4, 36.4, 32.1, and 33.8 (dB), respectively. The standard deviations of the phase differences between two adjacent depth scans of $\tilde{I}_{h0}$, $\tilde{I}_{v0}$, $\tilde{I}_{h1}$, and $\tilde{I}_{v1}$ of the sample were 0.016, 0.023, 0.062, and 0.059 (rad), respectively. This result is within the same order as that of the results of previous studies on phase-resolved SS-OCT systems [35, 38].

At this point, the phase fluctuations among each depth scan were cancelled, and only a constant phase offset remains. Equation (23) becomes identical for all depth scans. As a result, the effects of the phase fluctuations are cancelled by this calibration. After the calibration, the surface Jones matrices are averaged and applied to all the depth scans in the process of matrix

#92281 - $15.00 USD Received 30 Jan 2008; revised 22 Mar 2008; accepted 8 Apr 2008; published 11 Apr 2008

diagonalization. The spectra of the fixed pattern noise are obtained by averaging the spectra of $\tilde{I}_{h0}, \tilde{I}_{h1}, \tilde{I}_{v0}$, and $\tilde{I}_{v1}$ individually, and the former spectra are removed from the original spectra.

The schemes of the signal processing of PS-SS-OCT is summarized in a diagram shown in Fig. 3.

3. Results

3.1. Measurements of a quarter-wave plate and linear polarizer

In order to test the system after the calibration, a quarter-wave plate (QWP) and an LP (WPQ05M-1310 and LPNIR050, Thorlabs, Inc.) were measured individually. The orientation was rotated from 0° to 180° with a 10° increment, and 128 depth scans were averaged for each measurement. Figures 4 (a) and (b) show the double-pass phase retardation of the QWP and the double-pass diattenuation of LP, respectively. The averaged double-pass phase retardation of the QWP was $174 \pm 2^\circ$ and the averaged double-pass diattenuation of the LP was 0.97 ± 0.01. They were slightly lower than the expected values because of the wrapping effect of the noise near the edge of the range. The orientation relative to 0° is shown in Fig. 4 (c). The least squares fitted slopes of the QWP and LP were 0.99 ± 0.01 and 0.97 ± 0.01, respectively. The expected and measured orientations were in good agreement.

3.2. Measurements of biological samples

To demonstrate the potential of the system, we performed an *in vitro* measurement of chichen breast muscle. The intensity, phase retardation, and orientation images are shown in Fig. 5. A transversal scanning range of 1.6 cm was imaged with 512 axial scans. The intensity image with polarization diversity was calculated as $20\log\left\{\left(|\tilde{I}_{h0}| + |\tilde{I}_{v0}|\right)\right\}$. The fixed pattern noise, including the calibration mirror, was obtained by averaging the spectra in a B-scan image and it was removed from the image. Since the averaged surface Jones matrix was used as a reference to cancel the birefringence of the fiber-optic components, the phase retardation was zero at the surface of the B-scan. The phase retardation cyclically changed along the depth. The orientation had abrupt 90° shifts due to the phase wrapping at 180° phase retardation [39]. These images indicate that the system can measure the birefringence of the biological sample in the entire imaging range.

An *in vivo* human anterior eye segment was imaged by the system. Figure 6 shows the horizontally scanned images of the anterior chamber angle at the temporal side of an *in vivo* human right eye. The transversal scanning range of 5.0 mm (horizontal) $\times$ 4.7 mm (vertical) was imaged with 512×237 depth scans, where the fast scan was oriented in the horizontal direction and the slow scan in the vertical direction. The intensity image showed the corneal limbus, anterior chamber angle, iris, and sclera. The phase retardation was almost zero at the surface of the sample, except low-SNR region at the cornea. The non-zero phase retardation at the surface of the cornea was caused by the noise of the measured Jones matrix. The phase retardation image showed a highly birefringent area with approximately total 2π phase retardation (arrow). This feature was maintained in all the B-scans. According to our anatomical knowledge, we believe that this area corresponds to the trabecular meshwork, which has an important role in draining the aqueous flow. The cumulative phase retardation of the cornea and trabecular meshwork was projected on the iris. The projected phase retardation did not change in the iris, except in the iris pigment epithelium (IPE). The phase retardation of IPE was random and not consistent with the above region of the iris. The random appearance of birefringence, i.e., the so-called polarization scrambling, was clearly visible in the movie because the phase retardation did not have a correlation among the successive frames. Scleral birefringence was clearly observed in all the B-scans. These features of the phase retardation are in good agreement with those of a previous study conducted by Pircher et al. using time-domain PS-OCT [40].

#92281 - $15.00 USD Received 30 Jan 2008; revised 22 Mar 2008; accepted 8 Apr 2008; published 11 Apr 2008

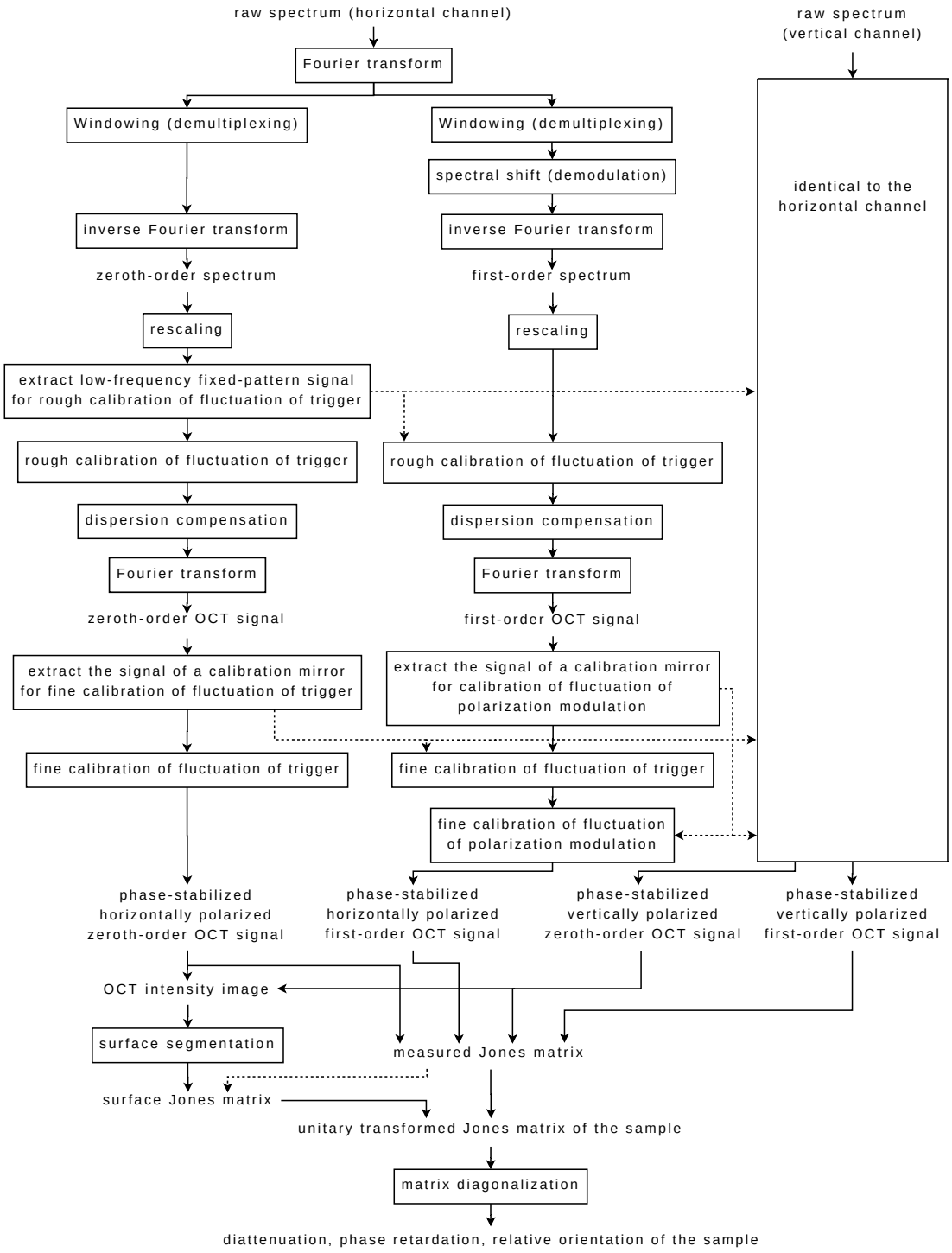

Fig. 3. Flowchart of the data processing. Since the process of the vertically polarized channel is almost the same as that of horizontally polarized channel, its description is abbreviated.

#92281 - $15.00 USD Received 30 Jan 2008; revised 22 Mar 2008; accepted 8 Apr 2008; published 11 Apr 2008

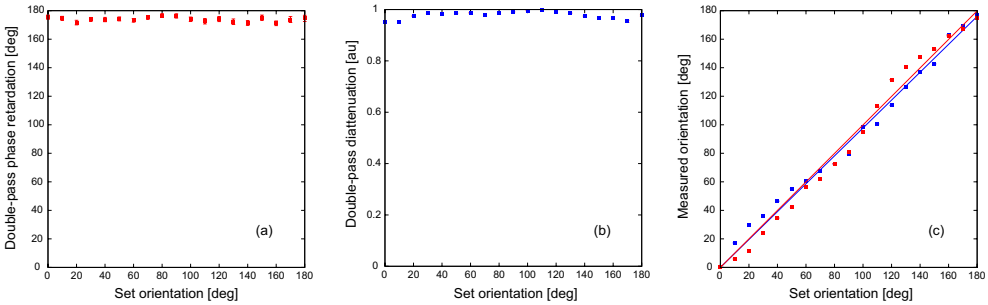

Fig. 4. (a) Double-pass phase retardation of the QWP, (b) double-pass diattenuation of the LP, and (c) relative orientation of the QWP and LP.

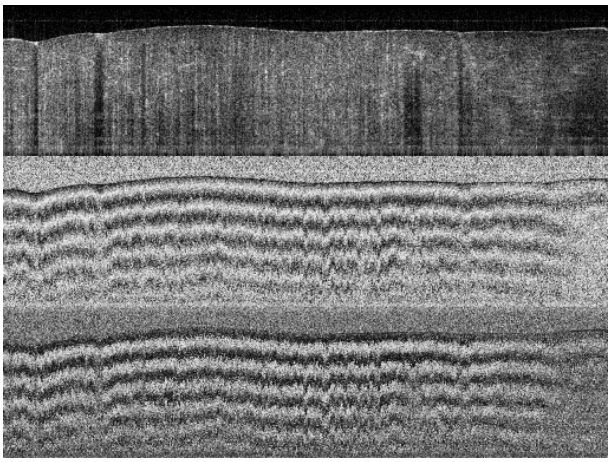

Fig. 5. Intensity (upper), phase retardation (middle) and orientation (lower) images of the chicken breast muscle. The image size is 1.6 cm (transversal) $\times$ 4.0 mm (axial) in air. The phase retardation image and the orientation image are indicated in gray scale from black (0°) to white (180° and 90°, respectively).

#92281 - $15.00 USD Received 30 Jan 2008; revised 22 Mar 2008; accepted 8 Apr 2008; published 11 Apr 2008

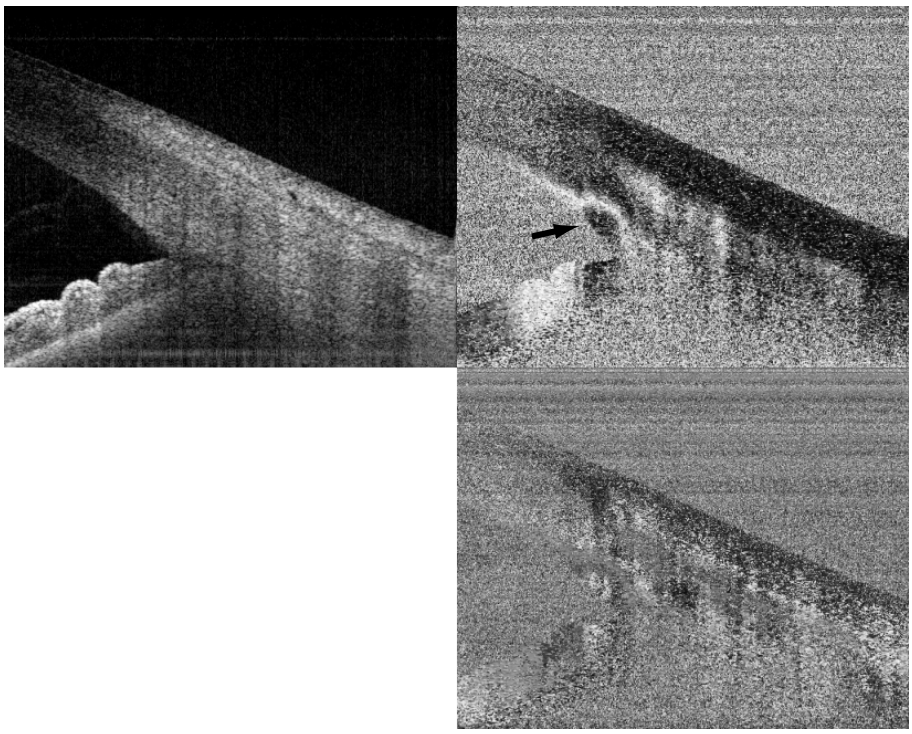

Fig. 6. Intensity (upper left), phase retardation (upper right) and orientation (lower right) images of the *in vivo* human anterior eye segment. The size of the images was 5.0 mm × 3.9 mm in air. (14.6 MB version).

4. Discussion

Our PS-SS-OCT system can measure the Jones matrices of the sample with frequency multiplexing of the polarization modulation. The algorithm was similar to the time-domain PS-OCT with continuous source polarization modulation [27] and the PS-SD-OCT with B-scan-oriented polarization modulation [31], except the frequency multiplexed detection of two polarization channels based on the continuous polarization modulation.

In our PS-SS-OCT system, the polarization-modulated light was fed into both the reference and sample arms. A different optical configuration would be possible by inserting the EOM into the sample arm. In this case, the same algorithm is applicable if we double the modulation voltage applied to the EOM. Although we have not employed this configuration due to a limitation in the RF amplifier, it is beneficial because the calibration of the PC and monitoring of the optical power in the reference arm are not required.

In the current setup, the depth range was shortened to one-third of the conventional SS-OCT. A direct method for extending the depth range is to increase the sampling frequency of the AD conversion. The other way is to optimize the modulation frequency. We can set the frequency of the polarization modulation at the Nyquist frequency of the data aquisition and suppress the first-order positive frequency image by a sharp electric low-pass filter. The remaining first-order negative frequency image can be used for processing the Jones matrix. With this configuration, the depth range can be extended up to half of what is achieved by the conventional SS-OCT. In this study, we use a sufficient margin to measure the entire first-order OCT signal.

#92281 - $15.00 USD Received 30 Jan 2008; revised 22 Mar 2008; accepted 8 Apr 2008; published 11 Apr 2008

When the sample is illuminated by 2.0-mW probing light and the backscattered light from the sample is evenly detected by the two photodetectors, the theoretical shot-noise-limited sensitivity [7] without polarization modulation is 115.2 dB. Assuming that there is no birefringence of the fiber-optic components and the sample and no phase fluctuation, the sensitivity of the zeroth-order OCT signal drops at -6 dB, which results in a sensitivity of 109.2 dB. The measured sensitivity is 101.7 dB at the depth of 566 μm. A dominant factor of the difference between the theoretical and measured values was probably the relative intensity noise due to an incomplete suppression by the balanced detection [41].

5. Conclusion

We have demonstrated that fiber-based PS-SS-OCT can be performed with continuous source polarization modulation. By extracting the zeroth-order and first-order OCT signals with respect to the frequency of the polarization modulation, the Jones matrix of the sample is measured with a single depth scan. The calibration method for canceling the phase fluctuations from the A-trigger and the timing between the data acquisition and the polarization modulation has been developed. The imaging of the anterior eye segment shows the ability of PS-SS-OCT to provide additional contrast that could not be imaged by conventional SS-OCT.

Acknowledgements

This research was supported in part by the grant from the Japan Science and Technology Agency and Grant-in-Aid for Scientific Research (15760026 and 18360029) from the Japan Society for the Promotion of Science (JSPS). S. Makita was supported in part by JSPS Research Fellowships for Young Scientists.

#92281 - $15.00 USD Received 30 Jan 2008; revised 22 Mar 2008; accepted 8 Apr 2008; published 11 Apr 2008